



# The 22 July 2020 $M_W$ 7.8 Shumagin seismic gap earthquake: Partial rupture of a weakly coupled megathrust



Lingling Ye<sup>a,b,\*</sup>, Thorne Lay<sup>c</sup>, Hiroo Kanamori<sup>d</sup>, Yoshiki Yamazaki<sup>e</sup>, Kwok Fai Cheung<sup>e</sup>

<sup>a</sup> Department of Earth and Space Sciences, Southern University of Science and Technology, Shenzhen, 518055, China

<sup>b</sup> Guangdong Provincial Key Lab of Geodynamics and Geohazards, School of Earth Sciences and Engineering, Sun Yat-sen University, Guangzhou, China

<sup>c</sup> Department of Earth and Planetary Sciences, University of California Santa Cruz, Santa Cruz, CA 95064, USA

<sup>d</sup> Seismological Laboratory, California Institute of Technology, Pasadena, CA 91125, USA

<sup>e</sup> Department of Ocean and Resources Engineering, University of Hawaii at Manoa, Honolulu, HI 96822, USA

## ARTICLE INFO

### Article history:

Received 29 September 2020

Received in revised form 27 February 2021

Accepted 7 March 2021

Available online xxxx

Editor: R. Bendick

### Keywords:

Shumagin gap

Alaska Peninsula earthquakes

seismic gaps

megathrust coupling

finite-fault inversion

## ABSTRACT

The earthquake potential of the Shumagin seismic gap along the Alaska Peninsula ( $\sim 162^\circ\text{W}$  to  $\sim 158.5^\circ\text{W}$ ) has been debated for more than 40 years. On 22 July 2020, the eastern half of the gap hosted an  $M_W$  7.8 earthquake involving a patchy rupture of the megathrust in the depth range of 20 to 45 km. The space-time slip distribution is determined by joint inversion of teleseismic  $P$  and  $SH$  waves and static displacements from regional GPS stations. The event initiated near the epicenter of the 10 November 1938 ( $M_W$  8.2) event, and ruptured westward, with little/no overlap with the 1938 rupture zone. The main slip patch has peak slip of  $\sim 3.8$  m below the Shumagin Islands, and produced  $\sim 30$  cm uplift and  $\sim 25$  cm SSE horizontal displacement on Chernabura Island. The slip model predicts well the small ( $< 1$  cm) tsunami signals persisting for more than ten hours observed at deep-water DART seafloor pressure recordings along the Alaska-Aleutian arc. Aftershocks with depths from 20 to 40 km fringe the large-slip patches, and show westward concentration during the first month after the mainshock. Aftershocks up-dip of the 1948  $M_W$  7.1 event contribute to the high level of modest-size background seismicity extending to the trench in the region of very low seismic coupling (0.0–0.1) in the western Shumagin gap east of the 1 April 1946 ( $M_W$  8.6) rupture zone. The 31 May 1917 event is the last major earthquake to rupture the eastern half of the Shumagin gap, and has a lower surface wave magnitude ( $M_{SG-R}$  7.4, horizontal components) compared to the 2020 event ( $M_{SG-R}$  7.7, vertical components). Comparison of instrument-equalized waveforms for the 1917 and 2020 events indicates similar size contrast and differences in overall rupture duration and slip complexity. The 2020 rupture has average slip of  $\sim 1.9$  m over the 3600 km<sup>2</sup> region with co-seismic slip  $\geq 1$  m. This is much less than the  $\sim 6.7$  m of potentially accumulated slip deficit since 1917, consistent with geodetic estimates of low average seismic coupling coefficient of 0.1–0.4. The megathrust seaward of the 2020 event has low seismicity and may either be aseismic or capable of comparable size ruptures. Comparisons are made with other subduction zones that have experienced relatively deep megathrust slip in regions with moderate seismic coupling.

© 2021 Elsevier B.V. All rights reserved.

## 1. Introduction

Almost the entire length of the Alaska-Aleutian subduction zone generates great earthquake ruptures such as the 1938 ( $M_W$  8.2), 1946 ( $M_W$  8.6), 1957 ( $M_W$  8.6), 1964 ( $M_W$  9.2) and 1965 ( $M_W$  8.7) events of the last century (e.g., Sykes, 1971; Sykes et al., 1981). Along the Alaska Peninsula from  $\sim 162^\circ\text{W}$  to  $\sim 158.5^\circ\text{W}$ ,

the Shumagin seismic gap has been identified as a megathrust segment located between the 1938 and 1946 rupture zones with potential for an earthquake as large as  $M_W$  8.3–8.5 with a recurrence interval of  $\sim 65$  years (Boyd et al., 1988). It could even involve an earthquake up to  $M_W$  9.0 (Davies et al., 1981), should it fail in conjunction with the 1946 tsunami earthquake rupture zone to the west and the adjacent Unalaska seismic gap up-dip along the easternmost extent of the 1957 rupture zone (e.g., House et al., 1981; Boyd and Jacob, 1986).

The seismogenic character of the Shumagin seismic gap (Fig. 1) was largely inferred from mainshock and aftershock relocations (Boyd and Lerner-Lam, 1988) and rupture analysis (Estabrook and

\* Corresponding author at: Department of Earth and Space Sciences, Southern University of Science and Technology, Shenzhen, 518055, China.

E-mail address: yell@sustech.edu.cn (L. Ye).

Boyd, 1992) of the 31 May 1917  $M_S$  7.4±0.3 event, which appears to have ruptured the easternmost Shumagin seismic gap region. The 1938 rupture initiated near the eastern margin of the gap, rupturing eastward, with most slip concentrated in the easternmost portion of the rupture zone (e.g., Boyd et al., 1988; Estabrook et al., 1994; Johnson and Satake, 1994, 1995; USGS, 2013). The western margin of the gap extends along the rupture zone of the 1946 tsunami earthquake (Kanamori, 1972), which appears to have ruptured the up-dip portion of the megathrust to near the trench (e.g., Johnson and Satake, 1997; Okal et al., 2002, 2003; Lopéz and Okal, 2006; Okal and Hébert, 2007). The smaller 14 May 1948 ( $M_W$  7.1) event (Fig. 1) appears to have ruptured the deeper portion of the central Shumagin gap (e.g., Sykes, 1971; Boyd et al., 1988; Estabrook et al., 1994). Moderate size thrust events in the gap include the 30 May 1991  $M_W$  6.9 (centroid depth 24.1 km from gCMT catalog;  $M_W$  7.0 from USGS-NEIC catalog; Figs. 1 and S1) and 13 May 1993  $M_W$  6.9 (centroid depth 40.7 km) earthquakes west of the 1917 rupture zone (e.g., Beavan, 1994; Estabrook et al., 1994; Lu et al., 1994; Tanioka et al., 1994) and a 14 February 1983  $M_S$  6.3 event seaward of the Shumagin Islands (Taber and Beavan, 1986). Smaller high stress drop events on 6 April 1974 ( $m_b$  5.8, 6.0) located on the deep megathrust have been reported by House and Boatwright (1980). The moderate size seismicity level in the gap is substantial, with activity in the western portion extending to the outer trench slope whereas the shallow megathrust of the eastern portion has little activity (Fig. S1). Prior ruptures spanning the Shumagin gap may have occurred in 1854 and in a pair of events on 22 July and 7 August 1788 that may have ruptured the eastern and western portions of the Shumagin gap, respectively (Solov'iev, 1968, 1990; Davies et al., 1981; Sykes et al., 1981; Lander, 1996). Nishenko and Jacob (1990) assigned a 60% conditional probability of a large earthquake occurring by 2008 in the Shumagin gap based on the assumption that the region failed in 1788, 1847, and 1917.

Questions have been raised about the size, nature and extent of faulting or landsliding in the 1854 and 7 August 1788 events (USGS, 2013). Witter et al. (2014) find no evidence for uplifted marine terraces or high tsunami along the coast of Simeonof Island in the Shumagin Islands, with only events producing less than 0.3 m uplift being allowed, which excludes great  $M \sim 9$  events. In contrast, field observations indicate large tsunami generation from the eastern end of the 1957 rupture zone, in the Unalaska gap region, suggesting that large slip did occur on the shallow megathrust there in 1957 (e.g., Witter et al., 2015; Nicolsky et al., 2016) rather than being concentrated in only the western part of the zone (e.g., Johnson and Satake, 1993, 1995). Large uplift of Sitkinak Island northeast of the 1938 rupture is consistent with slip extending that far east in the 22 July 1788 event, but the western extent of rupture is not well constrained (Briggs et al., 2014).

The identification of the Shumagin gap prompted extensive geodetic investigation. Tilt meters on the Shumagin Islands indicate a deep slow slip event in 1978–1979 (Beavan et al., 1983), with strong coupling inferred on the deeper portion of the megathrust from 1980–1988 (Beavan, 1988), although this was later refuted by lack of expected vertical deformation at regional tide gauges (Beavan, 1994). Early trilateration measurements across the Shumagin Islands failed to detect strain accumulation (e.g., Savage and Lisowski, 1986; Lisowski et al., 1988), but strain was indicated by initial differential GPS observations (Larson and Lisowski, 1994). Densification of GPS stations along the Alaska Peninsula and in the Shumagin Islands demonstrated a gradient from large slip-deficit accumulation along the strongly coupled 1938 zone to a weakly coupled Shumagin gap (e.g., Freymueller and Beavan, 1999; Fletcher et al., 2001; Fournier and Freymueller, 2007; Freymueller et al., 2008; Cross and Freymueller, 2008). The recent GPS analysis of megathrust coupling by Li and Freymueller (2018), infers

100% to 10% coupling decreasing with depth across the seismogenic zone in the eastern 1938 rupture zone, reduced coupling of 65% to 0% decreasing with depth in the western 1938 rupture zone, 45% to 25% coupling near the trench in the eastern Shumagin gap with 25% to 10% coupling beneath the islands, and <10% at greater depth, and 0% coupling at all depths in the western Shumagin gap (Fig. 1).

Trench-perpendicular seismic reflection profiles along the 1938 zone and the Shumagin seismic gap show sediment layers extending 40 km landward from the trench, thin reflectors at 50 km to 95 km from the trench, and deeper thick packages of reflections (Li et al., 2015). Shallow structure near the trench in the upper 10 km varies laterally, with landward dipping normal fault segments (Bécel et al., 2017; Von Huene et al., 2019) and a thinner layer of sediments along the Shumagin gap having lower pore pressure relative to the 1938 zone (Li et al., 2018). However, there is not a clear characterization of structural differences influencing the lateral gradient in seismic coupling at large depth. Hudnut and Taber (1987) observed a transition from a double Wadati-Benioff zone to a single zone going from west to east across the Shumagin Islands, which they attribute to a lateral gradient in megathrust coupling.

The eastern portion of the Shumagin gap ruptured in an  $M_W$  7.8 thrust event on 22 July 2020. This event provides a rare opportunity to evaluate large rupture of a megathrust region that appears to have weak seismic coupling. We determine the source process by analysis of seismic and geodetic data, confirming compatibility with the weak tsunami excitation that occurred, and compare waveforms with the 1917 event that likely ruptured the same portion of the gap to evaluate persistence of patches of slip accumulation.

## 2. Earthquake source characteristics

### 2.1. Point source parameters

The 22 July 2020 Shumagin earthquake hypocenter (06:12:44.7 UTC; 55.072°N, 158.596°W, 28.0 km depth; USGS-NEIC <https://earthquake.usgs.gov/earthquakes/eventpage/us7000asvb/executive>) is located at the eastern end of a ~225 km long by ~100 km wide aftershock zone that extends WSW along the ~300 km long Shumagin seismic gap (Fig. 1). A magnitude 5.5 normal faulting event occurred in the Pacific plate seaward of the western portion of the gap on 5 July 2020, but only a handful of small aftershocks for the 22 July event occurred near the trench. The USGS-NEIC reported 16 aftershocks with  $M_W \geq 5$  within 30 days, the largest being two  $M_W$  6.1 events. The Alaska Earthquake Center catalog (<http://earthquake.alaska.edu>) reported ~350 aftershocks with magnitude larger than 1.0 within one month (Figs. 2a and 7).

The USGS-NEIC  $W$ -phase moment tensor for the mainshock has a seismic moment  $M_0 = 6.919 \times 10^{20}$  N-m ( $M_W$  7.83), at a centroid depth of 23.5 km, with a half duration of 41.08 s. The solution has 87% double couple component, with the putative shallow-dipping fault plane having strike  $\phi = 232^\circ$ , dip  $\delta = 20^\circ$ , and rake  $\lambda = 73^\circ$ . The CMT moment tensor has  $M_0 = 7.38 \times 10^{20}$  Nm ( $M_W$  7.8), at a centroid depth of 36.3 km, with best double couple  $\phi = 243^\circ$ ,  $\delta = 17^\circ$ , and rake  $\lambda = 92^\circ$ , and 31.3 s centroid time shift and centroid location at ~50 km SW of the USGS-NEIC epicenter (Fig. 1). We perform a  $W$ -phase inversion (Kanamori and Rivera, 2008) using 271 seismograms from 106 global broadband stations filtered in the passband 0.002–0.01 Hz, finding a solution having  $M_0 = 6.92 \times 10^{20}$  Nm ( $M_W$  7.83) at a centroid depth of 35.5 km with best-double couple fault plane of  $\phi = 245.9^\circ$ ,  $\delta = 18.9^\circ$ , and  $\lambda = 96.1^\circ$ , and centroid time shift of 32 s. These shallow-dipping thrust fault solutions are very similar and quite well-constrained; we use the latter geometry in our finite-fault inversions.

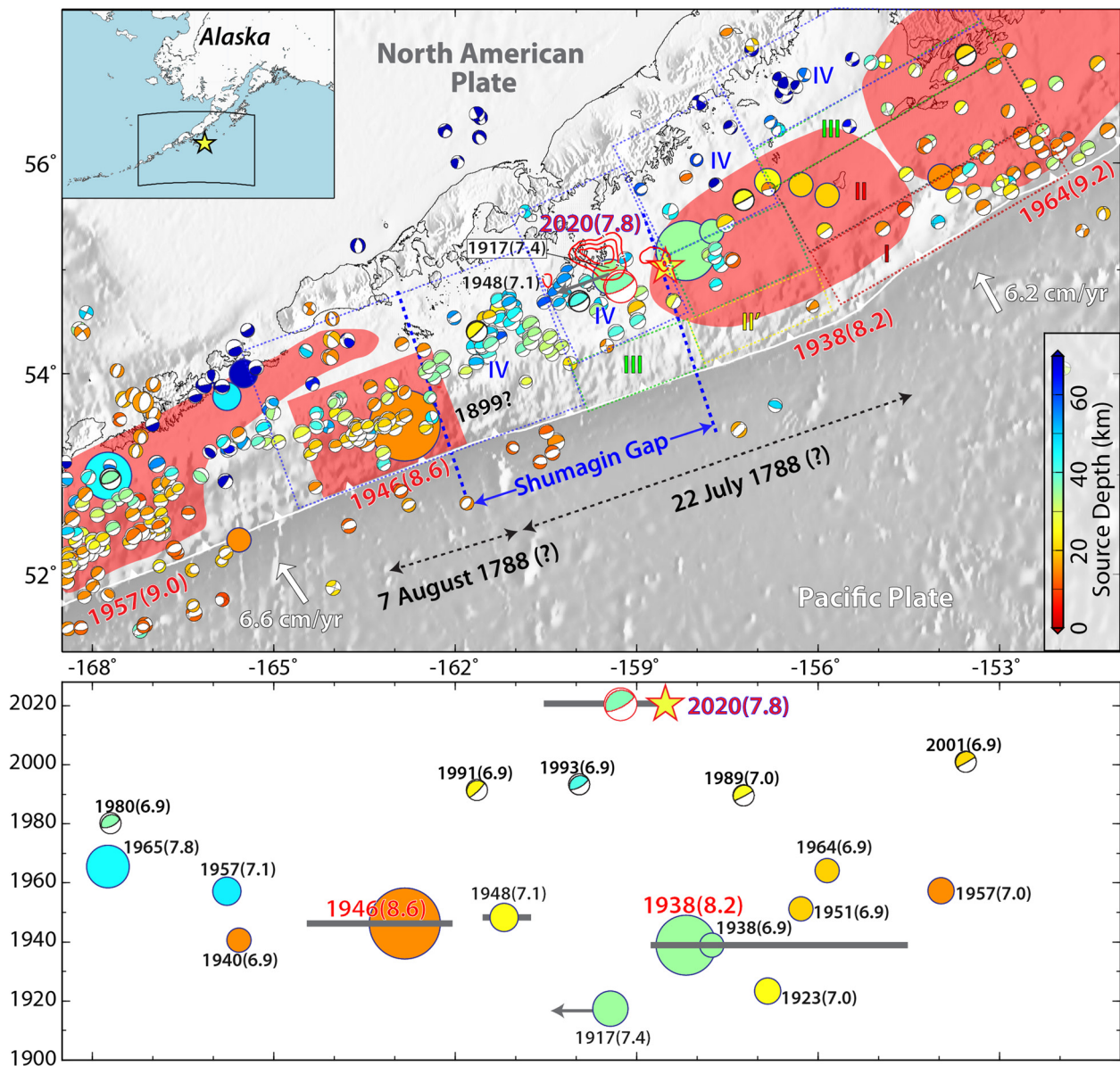


**Fig. 1.** Earthquake Seismicity of the Shumagin Islands region, Alaska. The 2020  $M_W$  7.8 earthquake slip pattern is outlined in red contours for regions with slip  $\geq 1$  m, and the yellow star shows the epicenter from USGS-NEIC. Focal mechanisms are from the Global Centroid Moment Tensor (GCMT) catalog from 1976 to 2020, color-coded by centroid depth. Large historical earthquakes from 1900 to 1975 with magnitude  $\geq 6.9$  from USGS-NEIC are shown by circles with size scaled by earthquake magnitude and color-coded by source depth. The light red areas indicate rupture zones for the historical great earthquakes of 1957 ( $M_W$  9.0), 1946 ( $M_W$  8.6), 1938 ( $M_W$  8.2) and 1964 ( $M_W$  9.2). The dark red (I), red (II), yellow (II'), green (III) and blue (IV) boxes indicate megathrust regions with 90%–100%, 40%–90%, 10%–40%, and 0–10% interface locking, respectively, approximated from Li and Freymueller (2018). Black dotted arrows indicate possible along-strike extent of two large earthquakes in 1788 (Davies et al., 1981). The map insert locates the Shumagin area along the Alaska Peninsula. The lower panel shows the time sequence of large earthquakes ( $M6.9+$ ) along longitude, with gray bars indicating their rupture extent and the gray arrow indicating the estimated rupture extent of the 1917 event (Estabrook and Boyd, 1992). (For interpretation of the figure, the reader is referred to the web version of this article.)

## 2.2. Finite source parameters

Back-projection of teleseismic 0.5–2.0 Hz  $P$  wave signals from large regional broadband networks in Greenland/Eurasia, North America/Caribbean, and Southeast Asia/Australia are performed using the procedure of Xu et al. (2009) to help constrain the source finiteness of the 2020  $M_W$  7.8 event. The locations of bursts of coherent short-period energy for the Greenland/Eurasia data track NW  $\sim 100$  km at  $\sim 3.0$  km/s from the hypocenter toward the Shumagin Islands for  $\sim 34$  s (Fig. S2a), with a second trend NNW aligned with strong smearing array response artifacts in the NNW direction. The data from North America have relatively low amplitude  $P$  waves in the first 40 s of the signals, and yield a scattered image with NE streaking artifacts (Fig. S2b). There are

NW and NNW trending distributions of short-period sources similar to those in the Greenland/Eurasia data. The data from Southeast Asia to Australia provide a fairly coherent trend of short-period radiators expanding at about  $3.0 \pm 0.3$  km/s NW across the Shumagin Islands, with no secondary NNW trend, and there is some WNW streaking in the image (Fig. S2c). The short-period  $P$  wave back-projections routinely produced by IRIS (<http://ds.iris.edu/spud/backprojection/18288679>) also suggest some NW migration of high-frequency release from North American and Eurasian networks and westward migration from an Australian network, but detail is not resolved. Overall, the back-projections indicate that the rupture did not propagate eastward or up-dip from the hypocenter, and expanded NW and possibly to the NNW with a rupture velocity of  $\sim 3.0$  km/s.

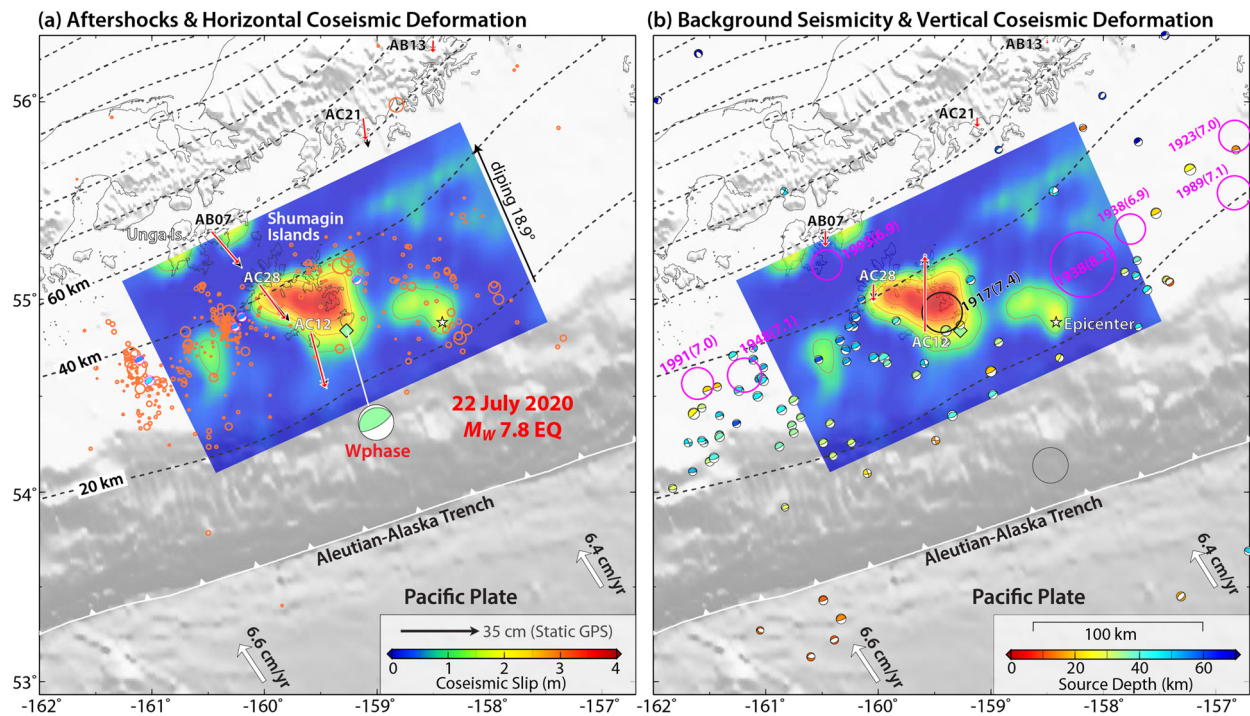


**Fig. 2.** Map view of the inverted slip model, geodetic observations and seismicity for the 2020  $M_w$  7.8 Alaska earthquake. (a) Comparison of the slip distribution with aftershock distribution and horizontal GPS static displacements. The brown circles are one-month aftershocks from the Alaska earthquake center (<http://earthquake.alaska.edu/>), with size scaled with earthquake magnitude. Black and red arrows show the observed and predicted horizontal co-seismic displacement at GPS sites, respectively. (b) Comparison of the slip distribution with the prior background seismicity from the GCMT catalog with focal mechanisms color-coded by source depth, and large historical earthquakes ( $M6.9+$ ) from USGS-NEIC (magenta circles). Black and red arrows show the observed and predicted vertical co-seismic displacement at GPS sites, respectively. The black-dashed curves in both (a) and (b) are 20 km depth contours of the slab interface model Slab2 (Hayes, 2018).

We determine the finite-fault slip model for the 2020 Shumagin gap event from teleseismic  $P$  and  $SH$  wave ground displacement seismograms and regional GPS static displacements using a linear least-squares kinematic inversion for a planar fault model with multiple rake-varying subfault source time function windows (e.g., Hartzell and Heaton, 1983; Kikuchi and Kanamori, 1991; Ye et al., 2016a). The seismic data are from global broadband network stations with good azimuthal distribution downloaded from the IRIS data center (<https://www.iris.edu/hq/>). The static displacements at nearby GPS sites AC12, AC28, AB07, AC21 and AB13 (Fig. 2) are 5-minute quick solutions of coseismic offsets determined by Nevada Geodetic Laboratory (<http://geodesy.unr.edu/>). The source region velocity structure used in the inversion is the local model from Crust 1.0 (Laske et al., 2013). Green's functions for the teleseismic signals are computed using a propagator matrix method for the layered structure, while those for the geodetic static deformation are computed using Okada (1985). A range of faulting geometries from the point-source inversions described above was explored, with the faulting extent and rupture expansion speed varied from 2.5 to 3.5 km/s, based on back-projection and waveform fitting. The surface motions from several GPS sites in the Shumagin Islands provide particularly strong constraint on the slip distribution.

For our preferred finite-fault model (Figs. 2 and 3), we specify the strike as  $245.9^\circ$  and the dip as  $18.9^\circ$  based on our  $W$ -phase inversion, with the rupture expansion speed being 3.0 km/s. The inversion uses 111  $P$  wave and 36  $SH$  wave ground displacements, bandpass filtered from 0.005 to 0.9 Hz. The hypocenter is set at 23 km deep based on the Alaska Earthquake Center catalog (<http://earthquake.alaska.edu/>). Subfaults of the model have dimensions of 10 km by 10 km, and the subfault source time functions are parameterized by 13 2-s rise time symmetric triangles offset by 2 s each, allowing up to 28 s rupture of each subfault. The actual subfault durations found in the inversion tend to be rather impulsive with durations of less than 10 s (Fig. 3). The average rake is  $90.2^\circ$ ,

and rake variations over the slip surface are minor. The moment rate function (Fig. 3a) has a total duration of  $\sim 71$  s, with a centroid time of 34.3 s and  $M_0 = 7.35 \times 10^{20}$  Nm ( $M_w$  7.84).

The slip model has two large-slip patches and a weaker patch located to the west along with some poorly resolved slip down-dip from the hypocenter and near the northwestern edge of the model (Fig. 2). The centroid depth of the slip distribution is 36.4 km, compatible with the 35.5 km depth of our  $W$ -phase inversion. The peak slip of  $\sim 3.8$  m is located in the slip patch below the Shumagin Islands, which has an area of about 2500 km<sup>2</sup> at depths of 25 to 45 km. The average slip is  $\sim 1.9$  m over an area of 3600 km<sup>2</sup> summed for regions with slip  $\geq 1$  m, and  $\sim 1.4$  m over an area of 6100 km<sup>2</sup> with a trimming factor of 0.15 relative to the peak slip subfault (slip  $\geq \sim 0.6$  m) (Ye et al., 2016a). The model matches the GPS horizontal and vertical static displacements well (Fig. S3; the RMS misfit is 2.74 cm), with  $\sim 25$  cm of south-southeast displacement and  $\sim 30$  cm uplift at the Chernabura site and downdrop at stations to the northwest, providing relatively good constraint on the placement of slip on the megathrust. Significant slip is not found at shallower depths than the hypocenter, even when models extending further seaward are considered (Fig. 2). While the hypocenter is located near the 1938 event hypocenter, rupture does not appear to extend into the 1938 rupture zone. The distribution of GPS observations is still limited, and absolute placement of slip has at least  $\sim 20$  km uncertainty horizontally. This uncertainty estimation is from the comparison with slip models derived from GPS-only (Crowell and Melgar, 2020) and from joint inversion of GPS, regional strong motion, and teleseismic observations (Liu et al., 2020), which give large-slip patches in very similar overall position with less than 20 km variation in the placement of large-slip patches along-strike and along-dip. The USGS-NEIC finite-fault model, based entirely on teleseismic observations has a somewhat patchy slip distribution (<https://earthquake.usgs.gov/earthquakes/eventpage/us7000asvb/finite-fault/>), with peak slip lo-

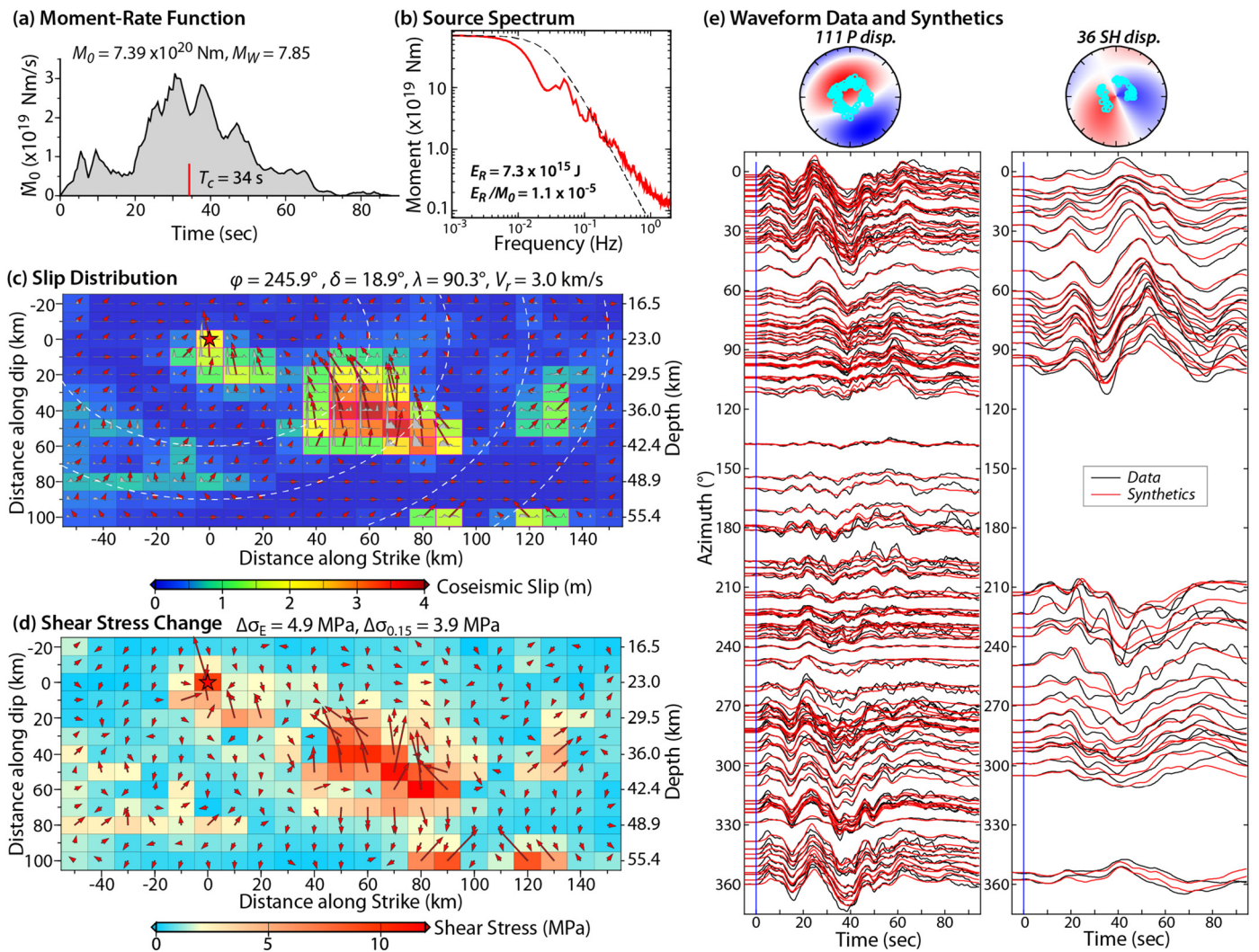


**Fig. 3.** Finite-fault rupture model for the 2020  $M_W$  7.8 Alaska earthquake obtained from joint inversion of teleseismic body waves and static GPS data. (a) The moment-rate function, with a red tick at the centroid time  $T_c$ . (b) Source spectrum inferred from the moment-rate function and teleseismic  $P$  wave spectra. (c) Slip distribution, with arrows showing the magnitude and direction of slip (hanging-wall relative to foot-wall) and subfaults color-coded by peak slip. The dashed white curves indicate the positions of the rupture expansion front in 10 s intervals. The subfault source time functions are shown within each subfault by gray polygons. (d) Shear stress change calculated from the slip distribution in a half space (Okada, 1985; Ye et al., 2016a). (e) Lower-hemisphere stereographic projections of the  $P$ -wave (left) and  $SH$ -wave (right) radiation patterns with raypath take-off positions for the data used in the inversion and comparisons of the observed (black) and predicted (red) waveforms for this model.

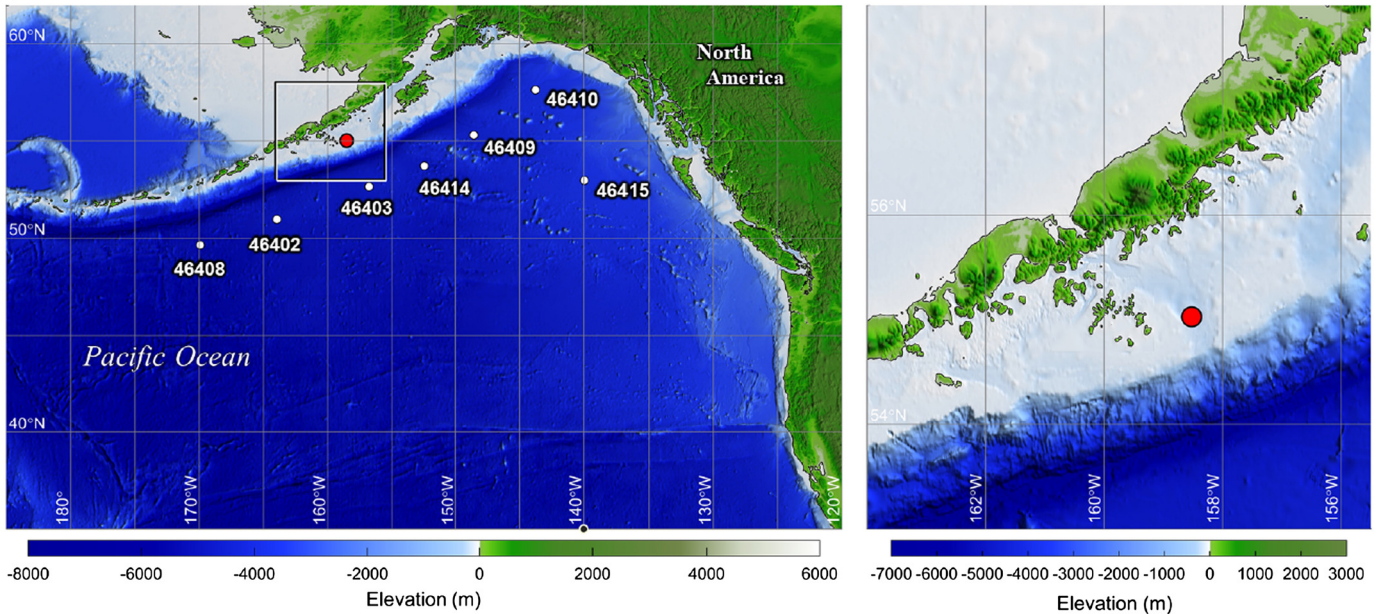
ated at the hypocenter, and several shallow slip patches along with some located to the northwest. Inclusion of the GPS observations significantly stabilizes the slip inversion, whereas models that include seismic data tend to have more slip near the hypocenter.

The source spectrum (Fig. 3b) is deeply notched near 0.02–0.03 Hz, which is related to the scale of the main slip patch, but shows gentle high-frequency decay with enhanced short-period radiation, possibly due to the depth of the slip (Lay et al., 2012; Ye et al., 2016b). We estimate a broadband radiated energy of  $E_R = 7.3 \times 10^{15}$  J, which combines contributions from the spectrum of the moment rate function for frequencies below 0.05 Hz with average broadband  $P$  wave spectra greater than 0.05 Hz corrected for radiation pattern and propagation. The moment-scaled radiated energy,  $E_R/M_0 = 1.05 \times 10^{-5}$ , which is close to the average ( $1.06 \times 10^{-5}$ ) for interplate thrust events found by Ye et al. (2016a). The slip-weighted stress drop  $\Delta\sigma_E = 4.9$  MPa, and the factor of 0.15 trimmed-slip circular stress drop estimate is  $\Delta\sigma_{0.15} = 3.9$  MPa (following Ye et al., 2016a), comparable to the average for megathrust events ( $\sim 3.4$ – $4.6$  MPa).

### 3. Tsunami records and modeling

Deep-water DART stations along the Alaska-Aleutian arc (Fig. 4a) recorded a small tsunami generated by the 2020  $M_W$  7.8 Shumagin earthquake (Fig. S4). These data have not been analyzed in the published finite-fault modeling papers. The weak signals, which are mixed with seismic-induced and background oscillations, lack sufficient signal-to-noise ratios for joint inversion or inclusion in iterative refinement of the seismo-geodetic inversion through forward tsunami modeling (Yamazaki et al., 2011b), but do provide an independent assessment of the preferred finite-fault model. We determine the time-histories of seafloor deformation for the slip model in Fig. 3 using the planar-fault solution of Okada (1985) and model the resulting tsunami using NEOWAVE of Yamazaki et al. (2009, 2011a). The depth-integrated non-hydrostatic model utilizes a telescopic system of two-way nested grids to describe multi-scale wave processes. Fig. 4a shows the two grid levels used in this study to resolve the tsunami source and trans-oceanic propagation at 0.5 and 2 arcsec, respectively. The high-resolution digital elevation model around the Shumagin Islands from NCEI blends in nicely with the surrounding GEBCO dataset. The model results

(a) Two levels of nested computational grids for tsunami modeling



(b) Computed tsunami amplitude

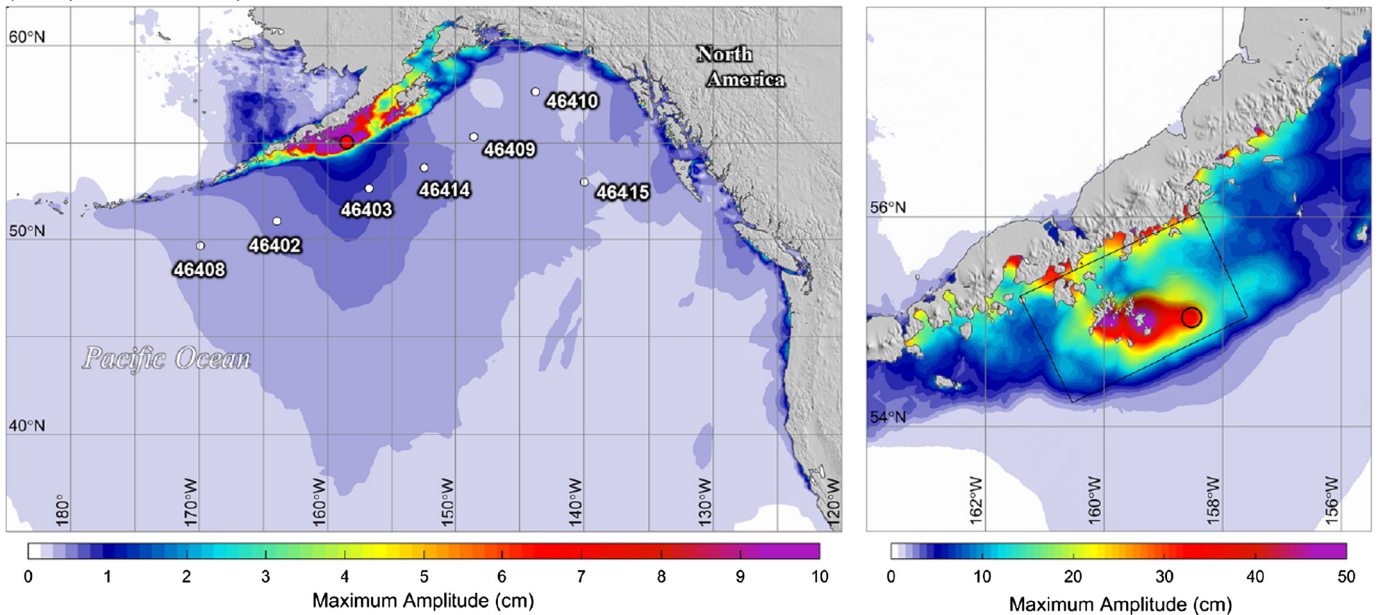


**Fig. 4.** Digital elevation model for tsunami simulation and computed maximum tsunami amplitude over the two levels of nested computational grids. (a) White circles and labels denote DART stations and numbers. Red dot indicates the earthquake epicenter. The box denotes the high-resolution grid region shown on the right. (b) Computed maximum tsunami amplitudes over the broad area and within the high-resolution area. The black rectangle delineates projection of the rupture zone on the continental shelf.

in Fig. 4b show concentration of energy with 10 cm or higher wave amplitude over most of the continental shelf. Radiated waves propagating down the continental slope undergo a reverse shoaling process with their amplitude reduced to less than 1 cm in the deep ocean, where the DART stations are located.

The continental shelf plays a significant role in the tsunami waves recorded at the DART stations. Video S1 illustrates the near-field wave processes. The initial sea-surface elevation is nearly identical to the vertical seafloor displacement, with the contribution from the horizontal displacement and non-hydrostatic effects being relatively small due to the shallow, gentle shelf (Fig. S5). The subsequent motion depends on the local bathymetry. East of the Shumagin Islands, the sea surface descends at higher rates over a submerged channel and banks of 200 m and 80 m depth.

The resulting waves of  $\sim 45$  min and  $\sim 70$  min period arrive at the Alaska Peninsula within an hour, coincidental with the uprush from the initial sea-surface drawdown. The Shumagin Islands exhibit a ring formation on a shallow shoal of less than 50 m depth that overlaps a significant portion of the initial uplift. The sea surface descends and rebounds slowly with a long period of  $\sim 110$  min for many hours due to wave trapping within the island formation. The predicted long-duration oscillation has been confirmed by GPS-interferometry that measures relative sea-level around the GPS receiver AC12 on Chernabura Island (Larson et al., 2021). The tsunami also triggers a number of edge wave modes over the shelf and the most prominent at  $\sim 90$  min period that can be inferred from the second half of the video when the most of the short-period energy has attenuated.

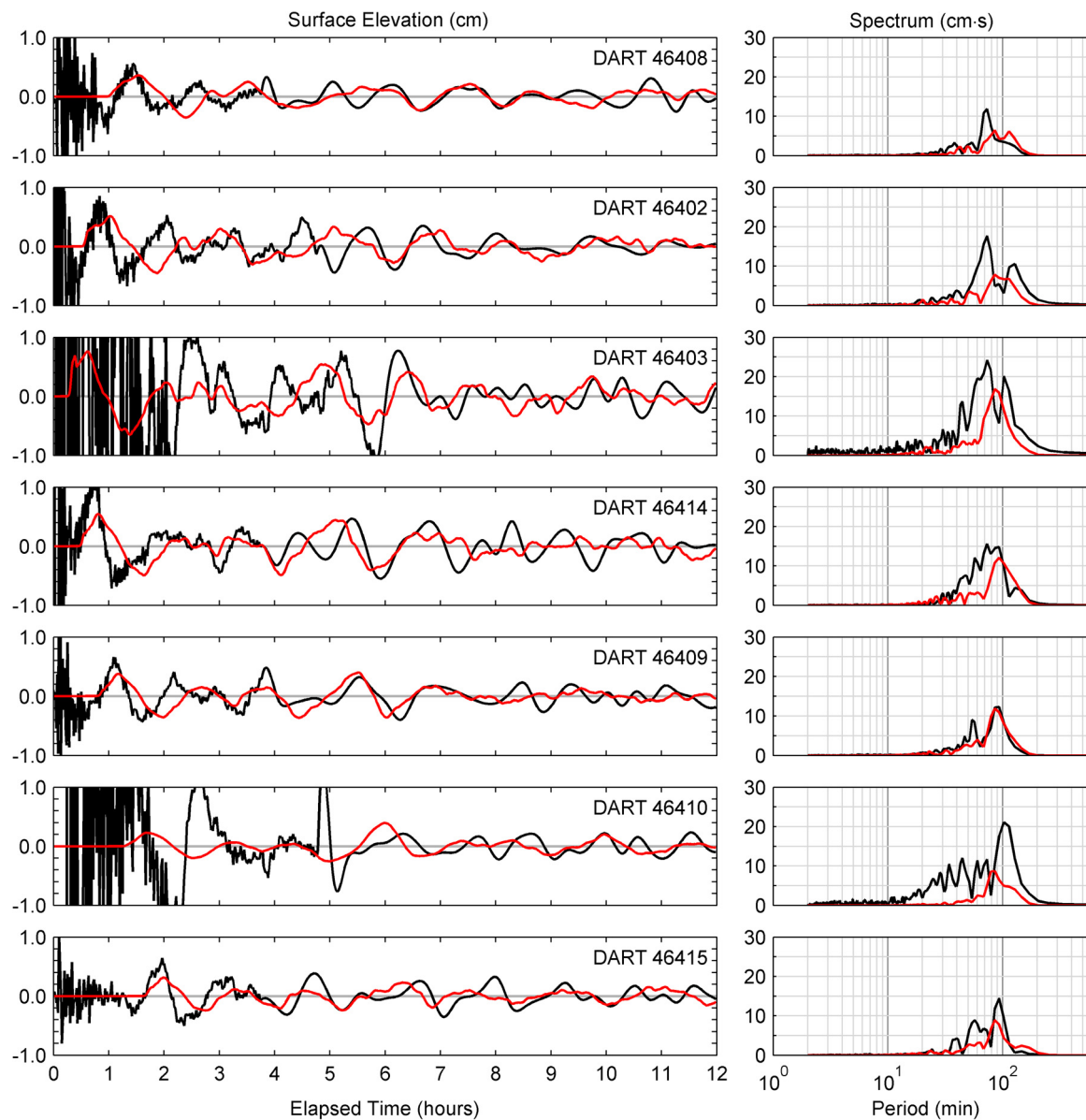


**Fig. 5.** Comparison of recorded (black lines) and computed (red lines) signals at DART stations along the Alaska-Aleutian arc. The stations are arranged from east to west with station 46403 nearest to the tsunami source (Fig. 4a). The sea surface elevation waveforms are shown in the left panels and their spectra versus period are shown in the right panels. Seismic-induced oscillations of 3 to 140 cm amplitude at the beginning of the time sequences are truncated for presentation of tsunami signals.

Analysis of the near-field tsunami wave pattern suggests the initial waves at the DART stations primarily come from the uplift east of the Shumagin Islands with periods of  $\sim 45$  min and  $\sim 70$  min, followed by their refraction-reflection along the continental margin and a steady supply of  $\sim 90$ -min and  $\sim 110$ -min waves leaked from oscillations over the continental shelf and the shallow shoal surrounded by the Shumagin Islands. These wave components coincide with the dominant resonance modes along the Alaska-Aleutian arc (Bai et al., 2015), which are evident in the DART data before the earthquake. The computed signals from the finite-fault model at the DART stations reproduce the long-period components and overall amplitude of the persistent oscillations, but underestimates the  $\sim 45$  and  $\sim 70$  min signals, leading to mismatch of the wave amplitude during the first few hours of the observations (Fig. 5). Increasing the epicentral uplift would augment the  $\sim 45$ -min and  $\sim 70$ -min signals to improve match of the DART records, but the joint slip inversion analysis constrains such adjustments. We found that the slip model from Liu et al. (2020), for which the slip patch extends  $\sim 20$  km south of our pre-

ferred model, produces almost identical waveform predictions at the DART stations. The strong interference with long-period noise level appears to be more influential than the precise slip placement. The tsunami model results lend support to the location and size of the major slip patch beneath the Shumagin Islands; additional data are needed to fully confirm or refine the source model.

#### 4. Discussion

The slip model shown in Figs. 2 and 3 has two to three patches of localized large-slip, but these do not fill the megathrust surface. The average slip of 1.4–1.9 m in the well-resolved portions of the model discussed above are only for the regions with coseismic slip  $\geq 0.6$ –1.0 m, and a very small area has a slip greater than 3 m. Fig. 6a shows 1-m contours of the slip model along with the first month of aftershocks from the Alaska Earthquake Center. These aftershocks tend to lie outside of the large-slip zones near the hypocenter, below the Shumagin Islands, and a small western

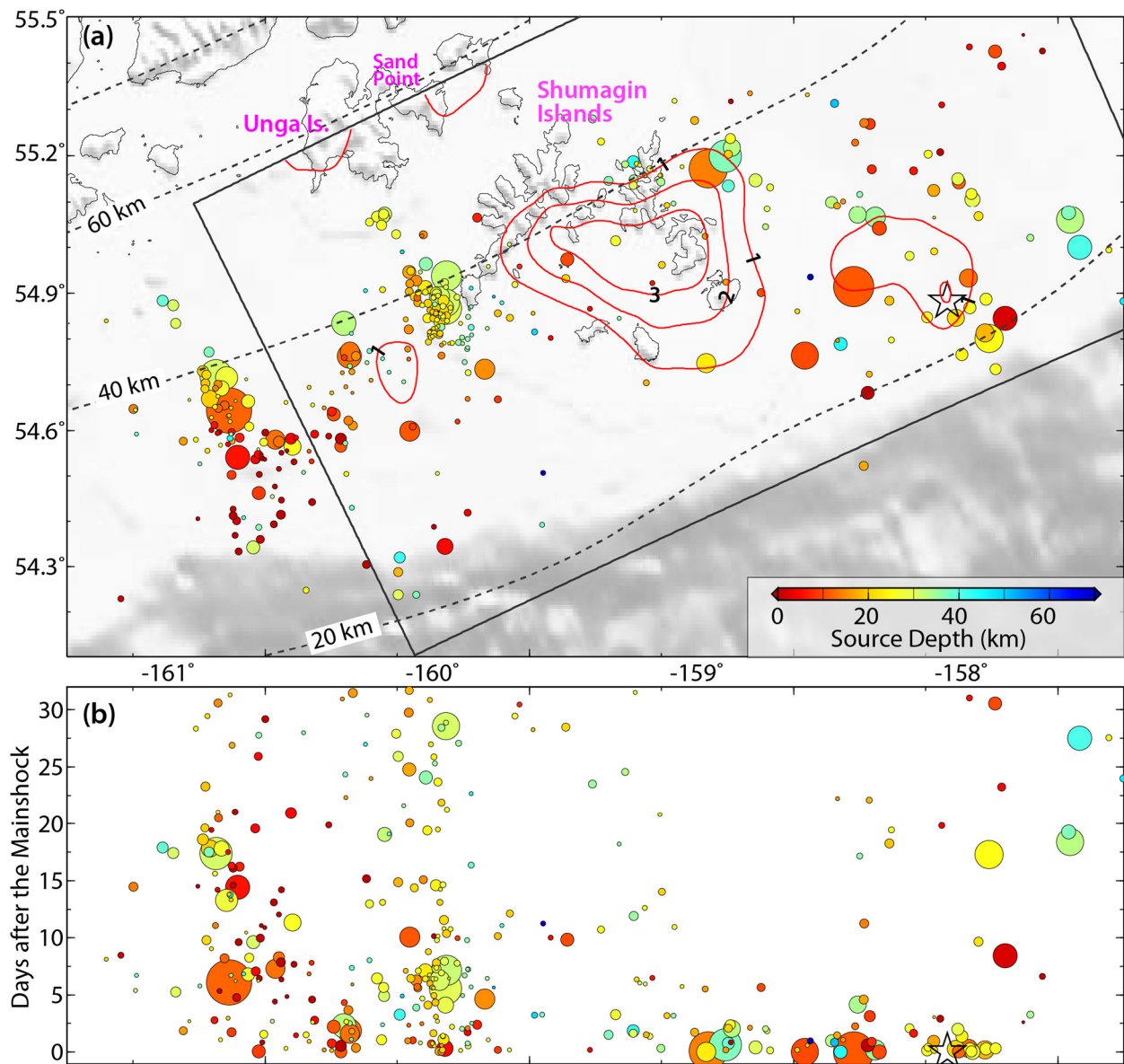


**Fig. 6. Spatial and temporal evolution of the aftershock sequence.** One-month aftershocks from the Alaska Earthquake Center (<http://earthquake.alaska.edu/>) are shown in circles with size scaled by earthquake magnitude and color-coded by source depth. The black box in (a) shows surface projection of the rupture model for the  $M_W$  7.8 mainshock along with 1-m slip contours (red).

slip patch, but they do not fill in shallow slip up-dip of the large slip patch, nor do they tend to extend deeper than  $\sim 40$  km. The aftershocks have a concentration westward from the coseismic slip distribution into the adjacent region of the Shumagin gap where the seismic coupling is very low. The entire sequence appears to partially rupture the eastern Shumagin gap with modest slip. The patchy nature of the slip and seismicity are compatible with the low value of seismic coupling inferred geodetically. While finite-fault inversions can underpredict peak-slip at very local scale, the data do exclude uniform slip of more than 1 m across the region. Assuming the last major slip event in the region was the 31 May 1917 earthquake, there are 103 years of potential strain accumulation which could have amounted to a 6.7 m slip deficit on local patches. That is much higher than we model even in the main slip patch.

The seismic observations for the 1917 and 2020 Shumagin earthquakes are compared in Fig. 7.  $M_{SG-R}$  measurements from horizontal components (classic Gutenberg-Richter  $M_S$  formula) are

plotted with azimuth in Fig. 7a. The 13 observations for 1917 are taken from Estabrook et al. (1994), who computed an average  $M_{SG-R} = 7.4 \pm 0.3$ . They noted that there is strong azimuthal variation and an early estimate of  $M_S = 7.9$  from a single station in Japan was biased by azimuthal sampling. For the 2020 event, measurements are made from vertical components using an updated  $M_S$  formula from Vanek et al. (1962), and there is again an azimuthal pattern with highest values to the northwest. The median value is  $M_{SG-R} = 7.73$  and a  $45^\circ$  azimuthally binned average value is  $M_{SG-R} = 7.74 \pm 0.19$  with median 7.69. Allowing for at most a minor increase ( $\sim 0.03$  unit) in magnitude due to use of vertical components (e.g., Lienkaemper, 1984), we infer that at  $\sim 20$  s period, the 2020 event is  $\sim 0.3$  magnitude units larger than the 1917 event.

Estabrook and Boyd (1992) compiled observations and instrument responses for the 1917 event and modeled several body waves and surface waves. To provide a straightforward comparison of  $P$  waves from the 1917 and 2020 events, we compare

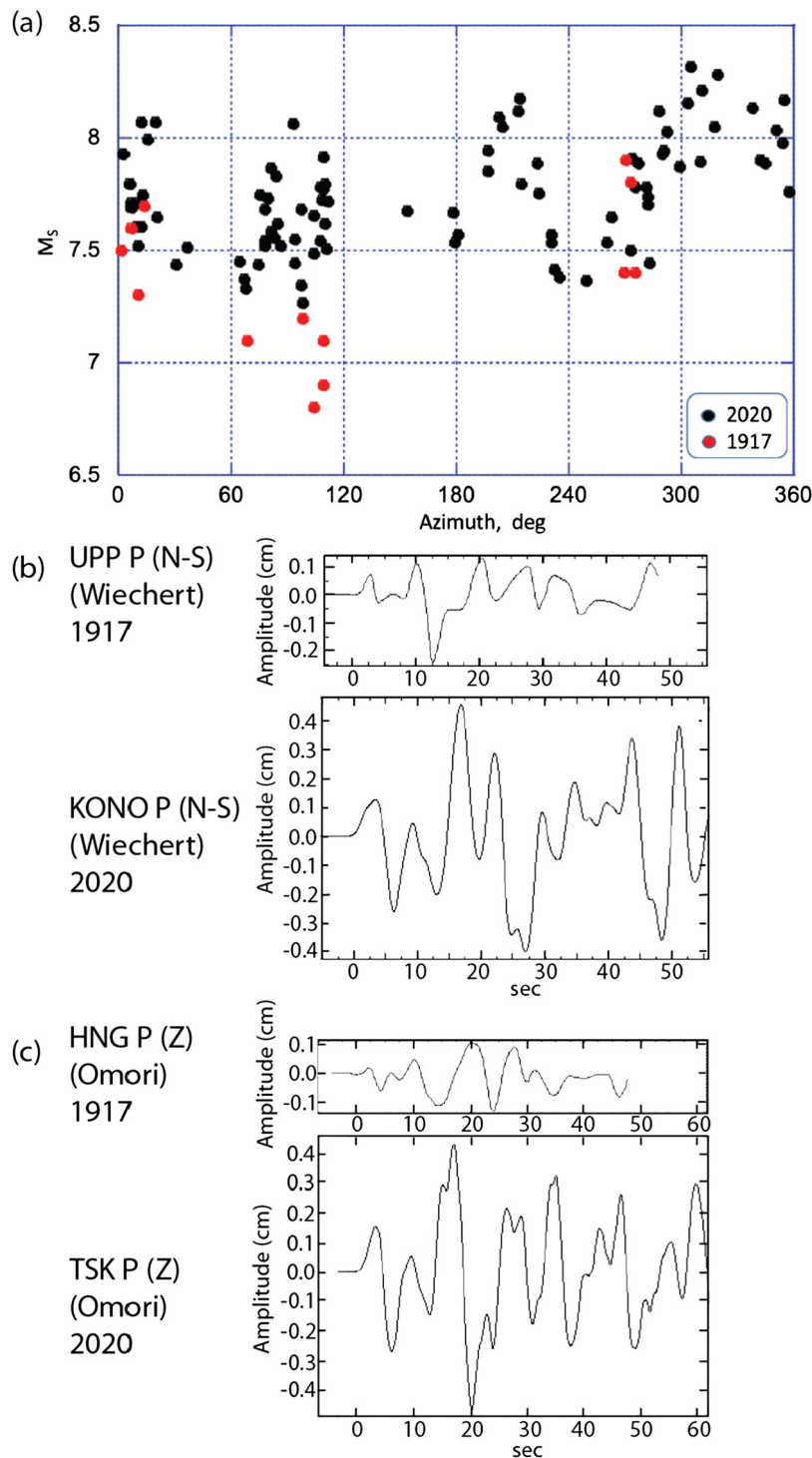


**Fig. 7. Comparison of seismic observations for the 1917 and 2020 Shumagin events.** (a)  $M_{SG-R}$  measurements using stations at different azimuths for the 1917 (black dots) and 2020 (red dots) earthquakes. (b) Comparison of P waves recorded at UPP on the Wiechert north-south component for the 1917 event and at KONO on the broadband north-south component equalized to the Wiechert response for the 2020 event (following the procedure in Ye et al., 2016c), with common amplitude scale. (c) Comparison of P waves recorded at HNG on the Omori vertical component for the 1917 event and at TSK on the broadband vertical component equalized to the Omori vertical response for the 2020 event, with common amplitude scale.

records from two stations that were particularly well-modeled by Estabrook and Boyd (1992). These are the Wiechert north-south component at station UPP (Uppsala, Sweden: 59.86°N, 17.62°E) and the Omori vertical component at station HNG (Hongo, Japan: 35.71°N, 139.77°E). Both of these are in stable positions in the thrust-faulting radiation pattern. Lacking co-located station recordings, we use nearby broadband recordings at KONO (Kongsberg, Norway: 59.64°N, 9.60°E); and TSK (Tsukuba, Japan: 36.21°N,

140.11°E) for the 2020 event, applying the Wiechert horizontal and Omori vertical responses to compare the waveforms (Figs. 7b and 7c). We use the instrument responses listed by Estabrook and Boyd (1992), replicating their plots of the instrument responses. Other body wave data they collected were considered, but are either near  $P$  or  $SH$  radiation nodes or have absolute amplitude uncertainties, making any comparison uncertain, so we rely on the two stable comparisons shown in Fig. 7.

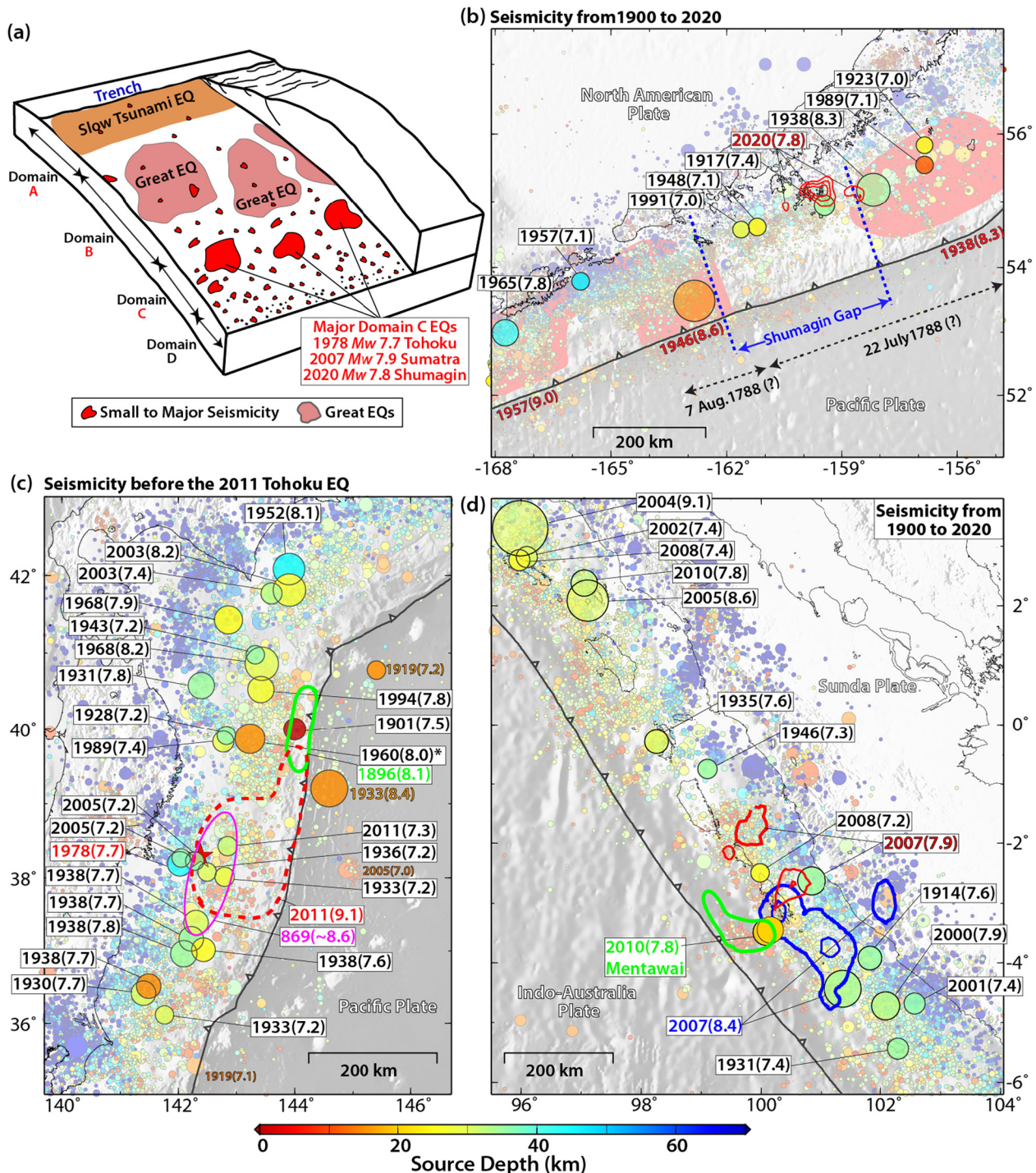


**Fig. 8.** Examples of subduction zone megathrusts with major earthquakes in the downdip Domain C section. (a) Schematic characterization of megathrust friction and rupture modified from Lay et al. (2012). (b)–(d) seismicity from the USGS-NEIC catalog for Alaska-Aleutian, off-shore Honshu, and Sumatra subduction zones, respectively. Circles are scaled with earthquake magnitude. Events with magnitude  $\geq 7.2$  are highlighted. The main slip distribution ( $\geq 1$  m) for the 2020  $M_W$  7.8 Shumagin (Fig. 4), 2007  $M_W$  7.9 Sumatra and 2007  $M_W$  8.4 Sumatra (Konca et al., 2008) earthquakes are shown by contours in (b) and (d). The red star and dashed line in (c) show the epicenter location and main slip area for the 2011  $M_W$  9.0 Tohoku earthquake. The estimated rupture areas of the 1896 Sanriku tsunami earthquake and 869 Jogan earthquake are shown in green and magenta, respectively. The 1960 Sanriku earthquake (asterisk) has  $M_{JMA} = 7.2$  (<https://ecatalogo.jma.es/en/>), and the  $M_W$  8.0 value in the USGS-NEIC catalog adopted from the ISC-GEM catalog is likely an overestimate due to limited azimuthal coverage.

The  $P$  wave form comparisons indicate that the 2020 earthquake is a factor of 3 to 4 larger than the 1917 event at periods of  $\sim 10$  s, basically consistent with the difference in  $M_{SG-R}$ . The waveshapes also differ significantly, and it appears the duration of large motions is greater for the 2020 event. This indicates that the rupture dynamics are probably quite different and it is not apparent that there are stationary slip patches contributing to both

ruptures, although more data would be required to resolve the space-time complexity of the 1917 event.

The 2020 Shumagin earthquake ruptured the deeper portion of the plate boundary interface, with most slip deeper than  $\sim 25$  km, which has been represented as Domain C in the depth-varying segmentation proposed by Lay et al. (2012) (Fig. 8a). Domain C events tend to rupture relatively localized slip patches that fail

in earthquakes with  $M_W < 8.0$ , while the shallower Domain B (~15–30 km deep) may or may not fail in larger events. With the small portion of the Shumagin gap that ruptured in the 2020 event (Fig. 8b), there is much uncertainty in the remaining seismic potential for the shallower portion of the megathrust along the gap, including the possibility of rupture of the near-trench Domain A, where tsunami earthquakes such as the 1946 Aleutian event (Fig. 8c) sometimes occur. The geodetic observations favor low seismic coupling on the interface in general, but lack resolution along dip. It is also challenging to constrain the overall behavior from the Domain C activity. This is demonstrated by consideration of the seismic behavior offshore of Honshu (Fig. 8c), notably around the 1978  $M_W$  7.7 Miyagi-oki earthquake. There were smaller ( $M_W$  7.2) nearby ruptures in 1933, 1936 and 2005, also in Domain C. The 1917–2020 Shumagin sequence has similar difference in size for ruptures of Domain C. The Miyagi-oki region subsequently failed as part of the plate boundary-wide (Domains A-B-C) 2011 Tohoku ( $M_W$  9.1) rupture, and may have failed in the 869 Jogan earthquake (Fig. 8c). This region has also had Domain A tsunami earthquakes, notably the 1896 event offshore Sanriku. Another example of a comparable size Domain C rupture is the 12 September 2007  $M_W$  7.9 Kepulauan, Sumatra earthquake (Fig. 8d), which followed a great ( $M_W$  8.4) megathrust event to the southeast on the same day. The region up-dip from the 2007 event ruptured in the 25 October 2010  $M_W$  7.8 Mentawai tsunami earthquake, which was confined to Domain A (Fig. 8d). A great earthquake rupture occurred in this area in 1797, plausibly spanning Domains A-B-C. These comparisons indicate that the behavior of Domain C ruptures is an unclear guide as to the shallower megathrust. Ongoing efforts to acquire GPS-Acoustic seafloor deformation seaward of the Shumagin Islands will help to shed light on the seismogenic potential of the shallower megathrust.

## 5. Conclusions

The 2020  $M_W$  7.8 Shumagin earthquake ruptured with a patchy slip distribution extending from 20 to 45 km depth in the eastern half of the seismic gap. There were at least 2 large-slip patches, the largest of which was located below the Shumagin Islands, with GPS recordings on the islands providing good constraint on the slip distribution in a joint inversion of teleseismic and GPS ground motions. The average slip in the well-resolved slip regions is less than 2 m, which is a small fraction of the potentially-accumulated slip deficit of ~6.7 m since the 1917  $M_{SG-R}$  7.4 earthquake rupture in the eastern Shumagin gap. The 1917 event appears to be about 0.3 magnitude units smaller based on comparison of surface wave measurements and instrument-equalized body waves. The patchy nature of the slip is compatible with geodetic estimates of modest (<0.4) seismic coupling coefficient for the eastern Shumagin gap. Recent inversion for seismic coupling coefficient from geodesy suggests that coupling may increase up-dip of the recent earthquake, possibly reaching a maximum near the trench. Viewing the 2020 event as a rupture of Domain C in the depth-varying subdivision of Lay et al. (2012), this raises the possibility that a large rupture could occur seaward of the recent event. Other regions such as along Honshu and along Sumatra have experienced ruptures of Domain C comparable to the Shumagin region, but have also experienced shallow tsunami earthquakes and great ruptures as well. Further efforts to establish the seismic coupling of the shallow interface are thus warranted.

## CRedit authorship contribution statement

LY performed finite-fault inversion and back-projection imaging; HK conducted  $W$ -phase inversion; YY performed the tsunami

data processing and modeling; LY, TL and HK conceived the project, and along with KC interpreted the results and wrote the manuscript collaboratively.

## Declaration of competing interest

The authors declare that they have no known competing financial interests or personal relationships that could have appeared to influence the work reported in this paper.

## Acknowledgements

Teleseismic body wave waveforms were downloaded from the Incorporated Research Institutions for Seismology (IRIS) data management center ([http://ds.iris.edu/wilber3/find\\_event](http://ds.iris.edu/wilber3/find_event)). Global Centroid Moment Tensor Solutions are from <https://www.globalcmt.org/CMTsearch.html>. Earthquake information is based on the catalogs from National Earthquake Information Center at U.S. Geological Survey (USGS-NEIC) (<https://earthquake.usgs.gov/earthquakes>) and Alaska Earthquake Center (<http://earthquake.alaska.edu>), last accessed on August 26, 2020. The high-resolution digital elevation model, Sand Point V2, at the Shumagin Islands was downloaded from the Nation Centers for Environmental Information (<https://maps.ngdc.noaa.gov/viewers/bathymetry/>). We thank Professor Jeff Freymueller for helpful comments on the manuscript. Lingling Ye's earthquake study is supported by National Natural Science Foundation of China (No. 41874056, 41790465, and U1901602). Thorne Lay's earthquake research is supported by National Science Foundation (Grant EAR1802364) and Yoshiki Yamazaki and Kwok Fai Cheung received support for tsunami hazard assessment from the National Oceanic and Atmospheric Administration (Grant NA19NWS4670012).

## Appendix A. Supplementary material

Supplementary material related to this article can be found online at <https://doi.org/10.1016/j.epsl.2021.116879>.

## References

- Bai, Y., Yamazaki, Y., Cheung, K.F., 2015. Interconnection of multi-scale standing waves across the Pacific from the 2011 Tohoku tsunami. *Ocean Model.* 92, 183–197.
- Beavan, J., 1988. Crustal deformation in the Shumagin seismic gap, Alaska. U.S. Geological Survey Open-File Report 88-673, pp. 183–188.
- Beavan, J., 1994. Crustal deformation measurement in the Shumagin seismic gap, Alaska. U.S. Geological Survey Open-File Report 94-176, pp. 195–205.
- Beavan, J., Hauksson, E., McNutt, S.R., Bilham, R., Jacob, K.H., 1983. Tilt and seismicity changes in the Shumagin seismic gap. *Science* 222, 322–325.
- Bécel, A., Shillington, D.J., Delescluse, M., Nedimovic, M.R., Abeers, G.A., Saffer, D.M., Webb, S.C., Keranen, K.M., Roche, P.-H., Li, J., Kuehn, H., 2017. Tsunamigenic structures in a creeping section of the Alaska subduction zone. *Nat. Geosci.* 10, 609–613.
- Boyd, T.M., Jacob, K., 1986. Seismicity of the Unalaska region, Alaska. *Bull. Seismol. Soc. Am.* 76, 463–481.
- Boyd, T.M., Lerner-Lam, A.L., 1988. Spatial distribution of turn-of-the-century seismicity along the Alaska-Aleutian arc. *Bull. Seismol. Soc. Am.* 78, 636–650.
- Boyd, T.M., Taber, J.J., Lerner-Lam, A.L., Beavan, J., 1988. Seismic rupture and arc segmentation within the Shumagin Islands seismic gap, Alaska. *Geophys. Res. Lett.* 15, 201–204.
- Briggs, R.W., Engelhart, S.E., Nelson, A.R., Dura, T., Kemp, A.C., Haeussler, P.J., Corbett, D.R., Angster, S.J., Bradley, L.-A., 2014. Uplift and subsidence reveal a nonpersistent megathrust rupture boundary (Sitkinak Island, Alaska). *Geophys. Res. Lett.* 41, 2289–2296.
- Cross, R.S., Freymueller, J.T., 2008. Evidence for and implications of a Bering plate based on geodetic measurements from the Aleutians and western Alaska. *J. Geophys. Res.* 113, B07405.
- Crowell, B.W., Melgar, D., 2020. Slipping the Shumagin gap: a kinematic coseismic and early afterslip model of the  $M_W$  7.8 Simeonof Island, Alaska, earthquake. *Geophys. Res. Lett.* 113, e2020GL090308.

- Davies, J., Sykes, L., House, L., Jacob, K., 1981. Shumagin seismic gap, Alaska Peninsula: history of great earthquakes, tectonic setting, and evidence for high seismic potential. *J. Geophys. Res.* 86, 3821–3855.
- Estabrook, C.H., Boyd, T.M., 1992. The Shumagin Islands, Alaska, earthquake of 31 May 1917. *Bull. Seismol. Soc. Am.* 82, 755–773.
- Estabrook, C.H., Jacob, K.H., Sykes, L.R., 1994. Body wave and surface wave analysis of large and great earthquakes along the eastern Aleutian arc, 1923–1993: implications for future events. *J. Geophys. Res.* 99, 11,643–11,662.
- Fletcher, H.J., Beavan, J., Freymueller, J., Gilbert, L., 2001. High interseismic coupling of the Alaska subduction zone SW of Kodiak island inferred from GPS data. *Geophys. Res. Lett.* 28, 443–446.
- Fournier, T.J., Freymueller, J.T., 2007. Transition from locked to creeping subduction in the Shumagin region, Alaska. *Geophys. Res. Lett.* 34, L06303. <https://doi.org/10.1029/2006GL029073>.
- Freymueller, J.T., Beavan, J., 1999. Absence of strain accumulation in the western Shumagin segment of the Alaska subduction zone. *Geophys. Res. Lett.* 26, 3233–3236.
- Freymueller, J.T., Woodard, H., Sohen, S.C., Cross, R., Elliott, J., Larsen, C.F., Hreindóttir, S., Zweck, C., 2008. Active deformation in Alaska based on 15 years of GPS measurements. In: Freymueller, J.T., Haeussler, P.J., Wesson, R.L., Ekström, G. (Eds.), *Active Tectonics and Seismic Potential of Alaska*. In: *Geophysics Monograph Series*, vol. 179. American Geophysical Union, Washington D.C., pp. 1–42.
- Hartzell, S.H., Heaton, T.H., 1983. Inversion of strong ground motion and teleseismic waveforms for the fault rupture history of the 1979 Imperial Valley California, earthquake. *Bull. Seismol. Soc. Am.* 73 (6A), 1553–1583.
- Hayes, G., 2018. Slab2 - a comprehensive subduction zone geometry model: U.S. Geological Survey data release. <https://doi.org/10.5066/F7PVGJNV>.
- House, L., Boatwright, J., 1980. Investigations of two high stress-drop earthquakes in the Shumagin seismic gap, Alaska. *J. Geophys. Res.* 85, 7151–7165.
- House, L.S., Sykes, L.R., Davies, J.N., Jacob, K.H., 1981. Evidence for a possible seismic gap near Unalaska Island in the eastern Aleutians, Alaska. In: Simpson, D.W., Richards, P.G. (Eds.), *Earthquake Prediction - An International Review*. Maurice Ewing Series 4. American Geophysical Union, Washington D.C., pp. 81–92.
- Hudnut, K.W., Taber, J.J., 1987. Transition from double to single Wadati-Benioff seismic zone in the Shumagin Islands, Alaska. *Geophys. Res. Lett.* 14, 143–146.
- Johnson, J.M., Satake, K., 1993. Source parameters of the 1957 Aleutian earthquake from tsunami inversion. *Geophys. Res. Lett.* 20, 1487–1490.
- Johnson, J.M., Satake, K., 1994. Rupture extent of the 1938 Alaskan earthquake as inferred from tsunami waveforms. *Geophys. Res. Lett.* 21, 733–736.
- Johnson, J.M., Satake, K., 1995. Source parameters of the 1957 Aleutian and 1938 Alaskan earthquakes from tsunami waveforms. In: Tsuchiya, Y., Shuto, N. (Eds.), *Tsunami: Progress in Prediction, Disaster Prevention and Warning*. Kluwer Academic Publishers, pp. 71–84.
- Johnson, J.M., Satake, K., 1997. Estimation of seismic moment and slip distribution of the April 1, 1946, Aleutian tsunami earthquake. *J. Geophys. Res.* 102, 11,765–11,774.
- Kanamori, H., 1972. Mechanism of tsunami earthquakes. *Phys. Earth Planet. Inter.* 6, 346–359.
- Kanamori, H., Rivera, L., 2008. Source inversion of W phase: speeding up seismic tsunami warning. *Geophys. J. Int.* 175, 222–238.
- Konca, A.O., Avouac, J.P., Sladen, et al., 2008. Partial rupture of a locked patch of the Sumatra megathrust during the 2007 earthquake sequence. *Nature* 456 (7222), 631–635.
- Kikuchi, M., Kanamori, H., 1991. Inversion of complex body waves—III. *Bull. Seismol. Soc. Am.* 81 (6), 2335–2350.
- Lander, J.F., 1996. *Tsunamis Affecting Alaska 1737–1996*. National Oceanic and Atmospheric Administration, Boulder, Colorado, National Geophysics Data Center. Key to Geophysical Research Documentation No. 31, 205 pp.
- Larson, K., Lisowski, M., 1994. Strain accumulation in the Shumagin Islands: results of initial GPS measurements. *Geophys. Res. Lett.* 21, 489–492.
- Larson, K.M., Lay, T., Yamazaki, Y., Cheung, K.F., Ye, L., Williams, S.D.P., Davis, J.L., 2021. Dynamic sea level variation from GNSS: 2020 Shumagin earthquake tsunami resonance and Hurricane Laura. *Geophys. Res. Lett.* 48, e2020GL091378.
- Laske, G., Masters, G., Ma, Z., Pasyanos, M., 2013. Update on CRUST1.0 - a 1-degree global model of Earth's crust. *Geophys. Res. Abstr.* 15, Abstract EGU2013-2658.
- Lay, T., Kanamori, H., Ammon, C.J., et al., 2012. Depth-varying rupture properties of subduction zone megathrust faults. *J. Geophys. Res., Solid Earth* 117 (B4).
- Li, S., Freymueller, J.T., 2018. Spatial variation of slip behavior beneath the Alaska Peninsula along Alaska-Aleutians subduction zone. *Geophys. Res. Lett.* 45, 3453–3460.
- Li, J., Shillington, D.J., Bécel, A., Nedimovic, M.R., Webb, S.C., Saffer, D.M., Keranen, K.M., Kuehn, H., 2015. Down-dip variations in seismic reflection character: implications for fault structure and seismogenic behavior in the Alaska subduction zone. *J. Geophys. Res., Solid Earth* 120.
- Li, J., Shillington, D.J., Saffer, D.M., Bécel, A., Nedimovic, M.R., Kuehn, H., Webb, S.C., Keranen, K.M., Abers, G.A., 2018. Connections between subducted sediment pore-fluid pressure and earthquake behavior along the Alaska megathrust. *Geology* 46 (4), 299–302.
- Lienkaemper, J.J., 1984. Comparison of two surface-wave magnitude scales:  $M$  of Gutenberg and Richter (1954) and  $M_S$  of "Preliminary determination of epicenters". *Bull. Seismol. Soc. Am.* 74, 2357–2378.
- Lisowski, M., Savage, J.C., Prescott, W.H., Gross, W.K., 1988. Absence of strain accumulation in the Shumagin seismic gap, Alaska, 1980–1987. *J. Geophys. Res.* 93, 7909–7922.
- Liu, C., Lay, T., Xiong, X., Wen, Y., 2020. Rupture of the 2020  $M_W$  7.8 earthquake in the Shumagin gap inferred from seismic and geodetic observations. *Geophys. Res. Lett.* 47, e2020GL090806.
- Lopéz, A., Okal, E.A., 2006. A seismological reassessment of the source of the 1946 Aleutian 'tsunami' earthquake. *Geophys. J. Int.* 165, 835–849.
- Lu, Z., Wyss, M., Tytgat, G., McNutt, S., Stihler, S., 1994. Aftershocks of the 13 May 1993 Shumagin Alaska earthquake. *Geophys. Res. Lett.* 21, 497–500.
- Nicolosky, D.J., Freymueller, J.T., Witter, R.C., Suleimani, E.N., Koehler, R.D., 2016. Evidence for shallow megathrust slip across the Unalaska seismic gap during the great 1957 Andreanof Islands earthquake, eastern Aleutian Islands, Alaska. *Geophys. Res. Lett.* 43, 10,328–10,337.
- Nishenko, S.P., Jacob, K.H., 1990. Seismic potential of the Queen Charlotte-Alaska-Aleutian seismic zone. *J. Geophys. Res.* 95, 2511–2532.
- Okada, Y., 1985. Surface deformation due to shear and tensile faults in a half-space. *Bull. Seismol. Soc. Am.* 75 (4), 1135–1154.
- Okal, E.A., Hébert, H., 2007. Far-field simulation of the 1946 Aleutian tsunami. *Geophys. J. Int.* 169, 1229–1238.
- Okal, E.A., Synolakis, C.E., Fryer, G.J., Heinrich, P., Borrero, J.C., Ruscher, C., Arcas, D., Guille, G., Rousseau, D., 2002. A field survey of the 1946 Aleutian tsunami in the far field. *Seismol. Res. Lett.* 73, 490–503.
- Okal, E.A., Plafker, G., Synolakis, C.E., Borrero, J.C., 2003. Near-field survey of the 1946 Aleutian tsunami on Unimak and Sanak Islands. *Bull. Seismol. Soc. Am.* 93, 1226–1234.
- Savage, J.C., Lisowski, M., 1986. Strain accumulation in the Shumagin seismic gap, Alaska. *J. Geophys. Res.* 91, 7447–7454.
- Solov'ev, S.L., 1968. Sanak-Kodiak tsunami 1788. In: *Problems Tsunami*. Nauka, Moscow, pp. 232–237.
- Solov'ev, S.L., 1990. Sanak-Kodiak tsunami of 1788. *Sci. Tsunami Hazards* 8, 34–38.
- Sykes, L.R., 1971. Aftershock zones of great earthquakes, seismicity gaps, and earthquake prediction for Alaska and the Aleutians. *J. Geophys. Res.* 76, 8021–8041.
- Sykes, L.R., Kissinger, J.B., House, L., Davies, J.N., Jakob, K.H., 1981. Rupture zones of great earthquakes in the Alaska-Aleutian Arc, 1784–1980. In: Simpson, D.W., Richards, P.G. (Eds.), *Earthquake Prediction - An International Review*. Maurice Ewing Series 4. American Geophysical Union, Washington D.C., pp. 73–80.
- Taber, J.J., Beavan, J., 1986. 14 February 1983 earthquake sequence in the Shumagin Islands, Alaska. *Bull. Seismol. Soc. Am.* 76, 1588–1596.
- Tanioka, Y., Satake, K., Ruff, L., González, F., 1994. Fault parameters and tsunami excitation of the May 13, 1993, Shumagin Islands earthquake. *Geophys. Res. Lett.* 21, 967–970.
- U.S.G.S., 2013. Alaska earthquake source for the SAFRR tsunami scenario. Open-File Report 2013-1170-B, California Geological Survey Special Report 229.
- Vanek, J., Zatopek, A., Karnik, V., Kondorskaya, N.V., Ryzhichenko, Y.V., Savarensky, E.F., Solov'ev, S.L., Shebalin, N.V., 1962. Standardization of magnitude scales. *Bull. Acad. Sci., USSR Geophys. Ser.*, 108–111.
- Von Huene, R., Miller, J.J., Krabbenhoef, A., 2019. The Shumagin seismic gap structure and associated tsunami hazards, Alaska convergent margin. *Geosphere* 15, 324–341.
- Witter, R.C., Briggs, R.W., Engelhart, S.E., Gelfenbaum, G., Koehler, R.D., Barnhart, W.D., 2014. Little late Holocene strain accumulation and release on the Aleutian megathrust below the Shumagin Islands, Alaska. *Geophys. Res. Lett.* 42, 2359–2367.
- Witter, R.C., Carver, G.A., Briggs, R.W., Gelfenbaum, G., Koehler, R.D., La Selle, S., Bender, A.M., Engelhart, S.E., Hemphill-Haley, E., Hill, T.D., 2015. Unusually large tsunamis frequent a currently creeping part of the Aleutian megathrust. *Geophys. Res. Lett.* 43, 76–84.
- Xu, Y., Koper, K.D., Sufri, O., Zhu, L., Hutko, A.R., 2009. Rupture imaging of the  $M_W$  7.9 12 May 2008 Wenchuan earthquake from back projection of teleseismic  $P$  waves. *Geochem. Geophys. Geosyst.* 10, Q04006.
- Yamazaki, Y., Cheung, K.F., Kowalik, Z., 2011a. Depth-integrated, non-hydrostatic model with grid nesting for tsunami generation, propagation, and run-up. *Int. J. Numer. Methods Fluids* 67 (12), 2081–2107.
- Yamazaki, Y., Kowalik, Z., Cheung, K.F., 2009. Depth-integrated, non-hydrostatic model for wave breaking and run-up. *Int. J. Numer. Methods Fluids* 61 (5), 473–497.
- Yamazaki, Y., Lay, T., Cheung, K.F., Yue, H., Kanamori, H., 2011b. Modeling near-field tsunami observations to improve finite-fault slip models for the 11 March 2011 Tohoku earthquake. *Geophys. Res. Lett.* 38 (7), L00G15. <https://doi.org/10.1029/2011GL049130>.
- Ye, L., Lay, T., Kanamori, H., Rivera, L., 2016a. Rupture characteristics of major and great ( $M_W \geq 7.0$ ) megathrust earthquakes from 1990–2015: 1. Source parameter scaling relationships. *J. Geophys. Res., Solid Earth* 121, 826–844.
- Ye, L., Lay, T., Kanamori, H., Rivera, L., 2016b. Rupture characteristics of major and great ( $M_W \geq 7.0$ ) megathrust earthquakes from 1990–2015: 2. Depth dependence. *J. Geophys. Res., Solid Earth* 121 (2), 845–863.
- Ye, L., Kanamori, H., Avouac, J.P., Li, L., Cheung, K.F., Lay, T., 2016c. The 16 April 2016,  $M_W$  7.8 ( $M_S$  7.5) Ecuador earthquake: a quasi-repeat of the 1942  $M_S$  7.5 earthquake and partial re-rupture of the 1906  $M_S$  8.6 Colombia–Ecuador earthquake. *Earth Planet. Sci. Lett.* 454, 248–258.